EMISSION SPECTROSCOPY OF LOW DENSITY AIR SHOCK TUBE FLOWS ABOVE 10 KM/S

Tobias Hermann, Peter Collen, Alex Glenn, Tamara Sopek, Matthew McGlivray, and Luca di Mare

*Hypersonics Group, Oxford Thermofluids Institute, University of Oxford, Southwell Building, Oseny Mead OX2 0ES
Oxford, United Kingdom*

1. INTRODUCTION

Interplanetary sample return missions require the re-entry into Earth's atmosphere with velocities well above 10 km/s. The heat load experienced by the entering vehicle is very high due to the heating of air by the strong compression shock in front of the capsule [And89]. As the flight velocity increases, the relative heating of radiation starts to dominate over the convective component [BJ14]. This typically starts to become significant above 10 km/s when excitation temperatures reach above 10,000 K leading to a high particle density of excited species, mostly present in atomic form. The uncertainty of the prediction of these heat loads is very high and therefore, these models require improvement [JMG+13], which can be achieved through experiments. Shock tube facilities replicate a small portion of a re-entry flowfield, namely the stagnation streamline, from undisturbed freestream through the shock layer. The flow can be idealised as one-dimensional and thus lends itself to the calibration and validation of simulation tools, as more complex flow features found in flows around bodies are excluded. Nevertheless, these flows exhibit a number of non-ideal effects such as shock deceleration [SGC+21], boundary layer effects [Mir66], radiative cooling [Pot11], travelling compression or expansion waves [SDMM21], shock deformation [BB19], gas impurity [CBJ17] etc. which complicates the interpretation of the data. The data from these experiments can serve different purposes, e.g numerical models can be validated or calibrated by comparing a CFD/radiation solution with a measured emission spectroscopic dataset [CB19], or measured radiative heat flux can be experimentally used to determine safety margins in numerical simulations intended for the design of re-entry vehicles [Joh20].

There are only few shock tube facilities world wide which can reach flight speeds relevant to hyperbolic re-entry. The largest openly available dataset is likely the emission spectroscopic dataset collected from the EAST facility at NASA Ames [BC17]. Recently, the Stalker tunnel T6 was commissioned in shock tube mode, utilising two different tube diameter options, 96.3 mm and 225 mm [CDS+21, GCM21, MDM+15]. The strong driver conditions of T6 enable high shock velocities while retaining a large tube diameter, providing a long optical path for a spectroscopic system. This enables a larger signal to noise ratio in the measurement of spectroscopic data while minimising exposure times in order to reduce the amount of spatial blurring due to shock movement. This study presents data of high speed shock tube flows at relatively low pressure, extending the available range of data currently available through comparable facilities around the world, e.g. [CMGO09, YTSF12, MEJ+11, LDSFR+20, KZB+21].

Table 1. Flow conditions tested. All shock tube fill pressures relate to ambient temperature of approximately 293 K. Shock velocity relates to the value obtained at the measurement location.

Shot	Fill pressure / Pa	Shock velocity / km/s
221	13.3	10.30
229	6.67	11.26
231	2.67	12.31

2. TEST CONDITIONS

The tested conditions are summarised in Table 1. They were obtained in the aluminium shock tube mode of T6 and using a secondary driver [CDS+21]. Main driver conditions were achieved using a 36 kg aluminium piston, a reservoir pressure of 2.6 MPa, a compression tube fill pressure of 35 kPa Helium, and a primary diaphragm rupture pressure of 46.2 MPa. A secondary driver was used with a fill pressure of 10 kPa Helium. The test gas was synthetic air, i.e. a mixture of 20.78% oxygen and 79.22% nitrogen, and was separated from the test gas by a 10 μm thick Mylar diaphragm. A comparison to existing data from the literature is presented in Fig. 1. The experimental measurements of the current work extend the available shock tube data in the open literature towards the high speed and low density regime. Shot 221 replicated conditions previously tested in the EAST facility, while Shots 229 and 231 provide new data at low shock tube fill pressures, relevant for high altitude trajectory points.

Shock speeds are determined experimentally by measuring the time of arrival of the travelling shock wave at various ’shock timing stations’, i.e. pressure transducers mounted in the tube wall. These data are treated in two ways to determine shock speed: The classical approach is used where the shock speed is determined between every adjacent pair of transducers. This implies that the shock travels at constant speed between each shock timing station, but could change its speed between the next pair. The uncertainty of this approach is determined using the methodology outlined in Ref. [JGL$^+$18]. One peculiar feature is that it leads to larger uncertainties if shock timing stations are placed closer to each other, which is a non-intuitive result. An alternative approach is based on the work in Ref. [CB19] where the shock velocity is determined by fitting a polynomial to the distance-time dataset of the shock timing stations and subsequently taking the time-derivative to determine velocity. Compared to the previous method, this approach prescribes a continuous functional shape to the shock and thus excludes sudden jumps in shock velocity between adjacent pairs of shock timing stations. More intuitively, this leads to smaller uncertainties if more closely spaced shock timing stations are used. The drawback is that the shock velocity profile is constrained to the chosen function, e.g. a polynomial. This approach is used here in combination with a Monte-Carlo uncertainty analysis where each shock timing station’s x and t values are randomly varied within their uncertainty bounds. The resulting x-t dataset is fitted with a polynomial of 4th degree and the shock velocity is determined along the shock tube. This procedure is repeated 10,000 times resulting in 10,000 velocity profiles. The standard deviation of these profiles is used as an uncertainty bound. The resulting plot using both methods is shown in Fig. 2. Due to the cross-sectional area change between shock timing stations 4 and 5, the shock speed is lower in the first third of the plot. As only the second half is relevant for the test gas, the polynomial fit is only carried out in this region. For larger distances between shock timing station pairs, the uncertainty of both methods is comparable. However, towards the end of the facility, a smaller uncertainty is calculated using the Monte-Carlo approach.

3. SPECTROSCOPIC SYSTEM

Shock layer radiation is collected through two 200 mm long opposing windows located on either side of the tube. The light is focussed onto the slit of a spectrograph using a telescopic imaging setup. Spectra were obtained in the wavelength regions 580 - 885 nm (VIS/NIR) using a 150 g/mm, and 210 - 440 nm (UV/VIS) using a 180 g/mm respectively with the two spectroscopic systems. A demagnification of 11.4 was achieved for the VIS/NIR system, and 20 for the UV/VIS side. Exposure times used in this study were 0.5 μs for both arrangements. This was chosen such that the signal to noise ratio was suf-

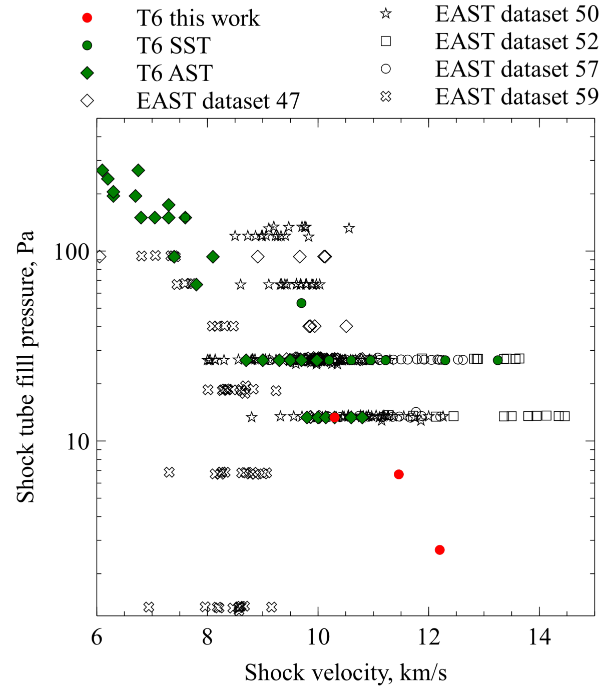

Figure 1. Flow conditions (air) tested. EAST conditions refer to Ref. [BC17], T6 flow conditions refer to Ref. [CDS$^+$21] for steel shock tube mode (SST) and Ref. [GCM21] for aluminium shock tube mdoe (AST).

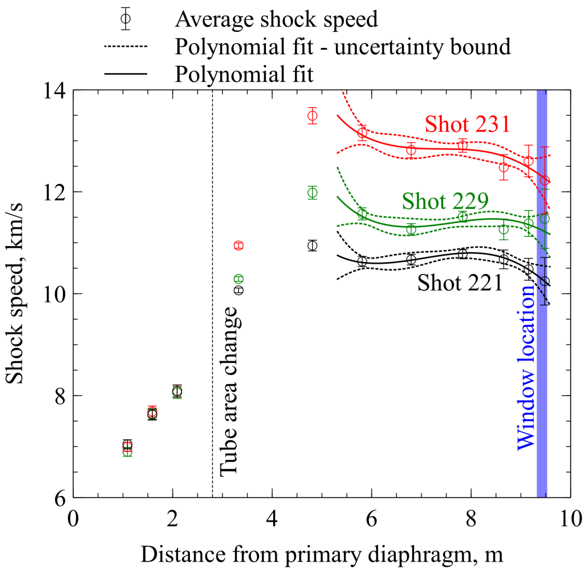

Figure 2. Shock speed along facility.

ficient while minimising motion blurring of the passing shock during the measurement. On the VIS/NIR side a Princeton Instruments Isoplane-320 spectrograph and an Andor Intensified sCMOS camera were used, while a McPherson 218 spectrograph and an Andor intensified sCMOS were used on the UV/VIS side. Details of the optical setups can be found in Refs. [CDM19, GCM21]. The collected radiation is calibrated for absolute spectral radiance using a Bentham Instruments SRS8 integrating sphere according to the methodology laid out in [Cru14]. In addition, a Deuterium lamp is used for lower wavelengths where the intensity of the integrating sphere is insufficient to result in a usable signal to noise ratio.

The experimental resolution is determined for both the spectral and spatial smearing functions. The spatial component is determined using an image where the edge of the integrating sphere is located in the centre of the spatial direction on the camera sensor. The spatial derivative of this edge location is calculated and an appropriate function from the NEQAIR 15.0 library is used [Cru14]. The best fit is achieved using a weighted Lorentzian and Gaussian function with full widths at half maximum of $\mathrm{FWHM}_{\mathrm{Gauss}} = 0.7\,\mathrm{mm}$, $\mathrm{FWHM}_{\mathrm{Lorentz}} = 0.5\,\mathrm{mm}$, and a weighting factor of $r = 5$. The spectral broadening function was assessed by measuring the emission of a mercury lamp providing thin atomic lines. The best fitting function was found to be a square root Voigt profile with $\mathrm{FWHM}_{\mathrm{Gauss}} = 1.253\,\mathrm{nm}$, $\mathrm{FWHM}_{\mathrm{Lorentz}} = 0.0087\,\mathrm{nm}$.

The collected data is compared to existing experimental datasets of the EAST facility [BC17, BJC16], and two computational codes, Poshax 3 and LASTA. Poshax3 is a one-dimensional numerical code calculating the non-equilibrium thermochemistry based on a transition from a frozen thermodynamic state to an equilibrated state [Gol08]. The model used in this study utilises a 3 temperature, 11 species dataset based on the Park 93 reaction rates [Par93]. Poshax3 is used with the nominal shock speed at the window location, and is able to compute a spatially resolved non-equilibrium profile. LASTA is a numerical tool capable of re-creating the enthalpy and pressure distribution behind a shock which has undergone a change in velocity over the run-time through the facility [SGC^{+}21]. This results in a spatially dependent thermodynamic equilibrium composition based on the measured attenuation of the shock velocity. Unlike Poshax3, LASTA takes the measured shock speed history along the tube into account, but does not account for non-equilibrium effects and thus only provides information about the local equilibrium composition. Finally, a zero-dimensional equilibrium composition is calculated using CEA2 based on the nominal shock speed and pressure at the window location [GM96]. The uncertainty bounds based on the shock speed Monte Carlo analysis are used to compute the upper and lower bounds of the expected equilibrium radiance profiles.

All determined flow compositions are subsequently parsed into NEQAIR 15.0 in order to calculate the spatially resolved emission spectrum [CB14]. Two different methods are used to determine the population distribution of excited states; a Boltzmann distribution and a flux-limited QSS-coupled model with a local escape factor approximation of 1 cm. Spatially resolved datasets are convolved with the measured spatial smearing function which also includes a square wave representing the motion blurring of the moving shock during the camera acquisition. Similarly, the spectral axis is convolved with the measured instrument function in order to compare experiment and simulation on a like-for-like basis. In the following, these data are compared to the experimental measurement, as well as comparable EAST datasets.

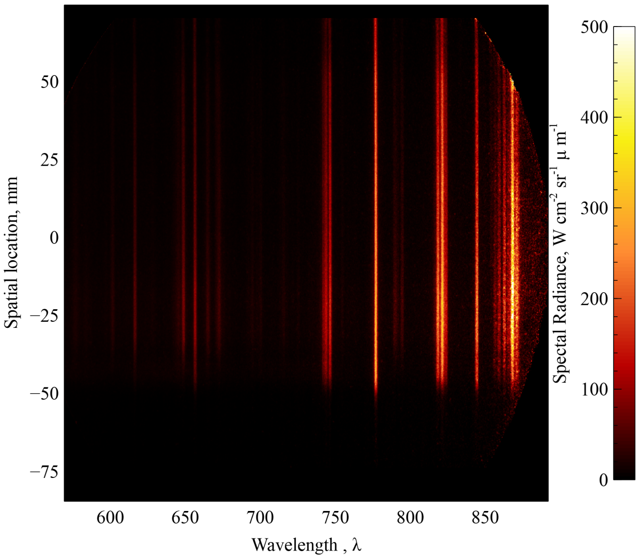

Figure 3. Spatially and spectrally resolved emission signal of shot 221.

3.1. Shot 221 - 10.30 km/s, 13.3 Pa

An example of an acquired spectrum is shown in Fig. 3 with the vertical axis denoting the spatial evolution of the shock and the horizontal axis denoting the spectral direction. The shock is moving from top to bottom. The spatial profile exhibits a plateau which has been spatially averaged to obtain the spectrum shown in Fig. 4. The emission consists mostly of atomic radiation stemming from oxygen and nitrogen in the visible and near infrared spectral region. Due to the very high enthalpies investigated in this work, molecules are almost fully dissociated, leaving only atomic lines as the remaining significant spectral features. A small contaminant line can be seen in the form of the Balmer-alpha Hydrogen line. In addition, an unknown contaminant is visible at 794 nm. The figure also contains simulation data which correspond to the same spatial location, as in the experimental region. Cumulative radiance is shown only from 680-850 nm to exclude the influence of the Balmer-alpha line and higher wavelengths where the calibration exhibits larger uncertainty.

This condition in particular lends itself to a direct com-

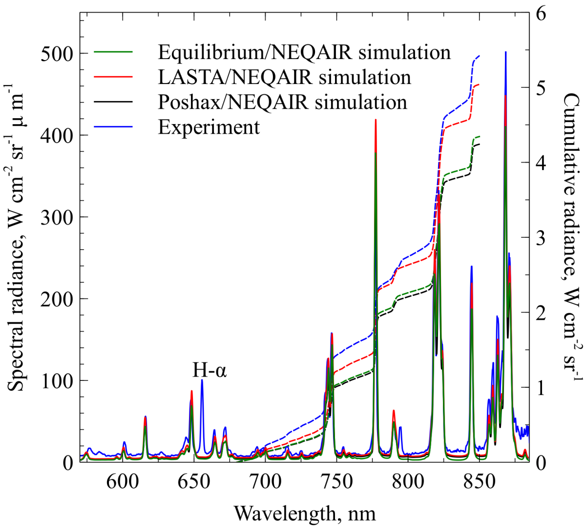

Figure 4. Spectrum of shot 221 averaged between 40 and 60 mm. Dashed lines correspond to cumulative radiance.

parison to similar data obtained in the EAST facility, due to the availability of several almost identical conditions. Figure 5 shows a compilation of integrated (between 680 nm and 850 nm) radiance profiles and their respective equilibrium values. All experimental data refers to a nominal shock tube fill pressure of 13.3 Pa. Even though, the variance in shock speed is not large, a big difference in absolute radiative intensity is observed with higher speed shocks producing stronger radiation. The same dataset is shown in Fig. 6 where each profile is normalised by its respective equilibrium value obtained by a CEA simulation using the nominal shock speed at the measurement location. It shows that most profiles exhibit a common feature in the non-equilibrium region, a slight peak before a slower rise to the equilibrium region. A great variance exists in profiles with regards to the strength of the non-equilibrium peak. Furthermore, the decay of radiation after the steady plateau of the equilibrium region starts at different locations, indicating different test times between the investigated conditions. The same phenomenon is also visible in other wavelength regions, as shown in Ref. [BC17] for numerous high speed conditions.

The radiation collected from T6 exceeds its predicted equilibrium value at its highest peak, while some EAST tests under-predict the expected equilibrium radiation. The spatial profile of shot 221 also exhibits the initial rise, however it is more blurred out compared to the data from EAST. This is likely due to the telescopic optical arrangement in T6 which tends to suffer from a larger spatial smearing function than the telecentric EAST system. This is also reflected in the smeared radiance profile ahead of the shock. The length of the non-equilibrium region is similar to the EAST data reaching an equilibrium plateau after approximately 20 mm. The qualitative similarity between facilities is especially good for EAST

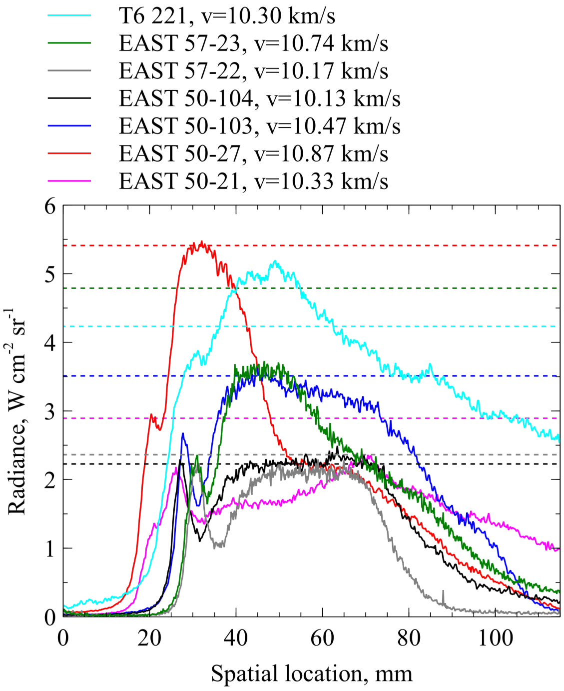

Figure 5. Integrated radiance between 680 nm and 850 nm. Dashed lines correspond to each respective equilibrium calculation obtained using CEA and NEQAIR.

50-27 and 57-23 which show very similar features compared to the T6 dataset.

Figure 7 shows the simulation results relating to shot 221. It shows the measured radiance profile, and the aforementioned computational simulations. The identified equilibrium region is significantly above the predicted equilibrium value and is just at the edge of the upper uncertainty bound. This may be due to the shock deceleration prior to the window measurement location. This is also reflected in the LASTA analysis which shows a rising radiance profile over the nominal equilibrium value. However, LASTA predicts a slower rise than the measurement data. However, LASTA doe not include non-equilibrium effects. These are included in the two Poshax simulations. However, these simulations do not include the shock speed variation along the tube. It is evident that the population distribution plays a major role in the spatial radiance profile. The Boltzmann distributed radiance strongly over-predicts the non-equilibrium region, while the non-Boltzmann model does not capture the double peak characteristic adequately.

The numerical spectra reveal that the double peak is caused by strongly overpopulated N_2 high energy states while the experimental data shows no discernible trace of molecular radiation. The slower rise after this first region is predicted to be due to atomic lines. Predicted atomic non-Boltzmann distributions exhibit depletion of very high energy states near the ionisation limit, likely due to ionisation reactions. Furthermore, energy states above approximately 10,000 cm^{-1} exhibit a notably dif-

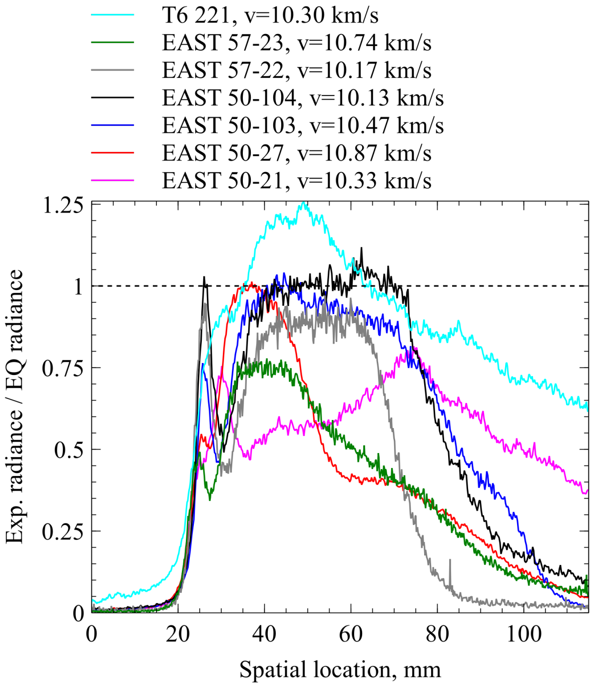

Figure 6. Integrated radiance between 680 nm and 850 nm divided by its respective equilibrium value. Dashed line correspond to equilibrium calculation obtained using CEA and NEQAIR. Note that the shock starting location has been adjusted for easier comparison.

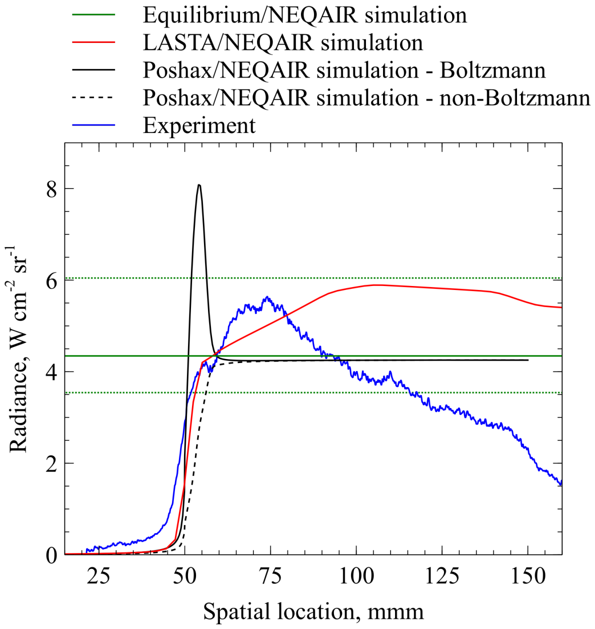

Figure 7. Spatially resolved integrated radiance between 680 nm and 850 nm for shot 221. Green dotted lines denote equilibrium radiance taking shock speed uncertainty into account.

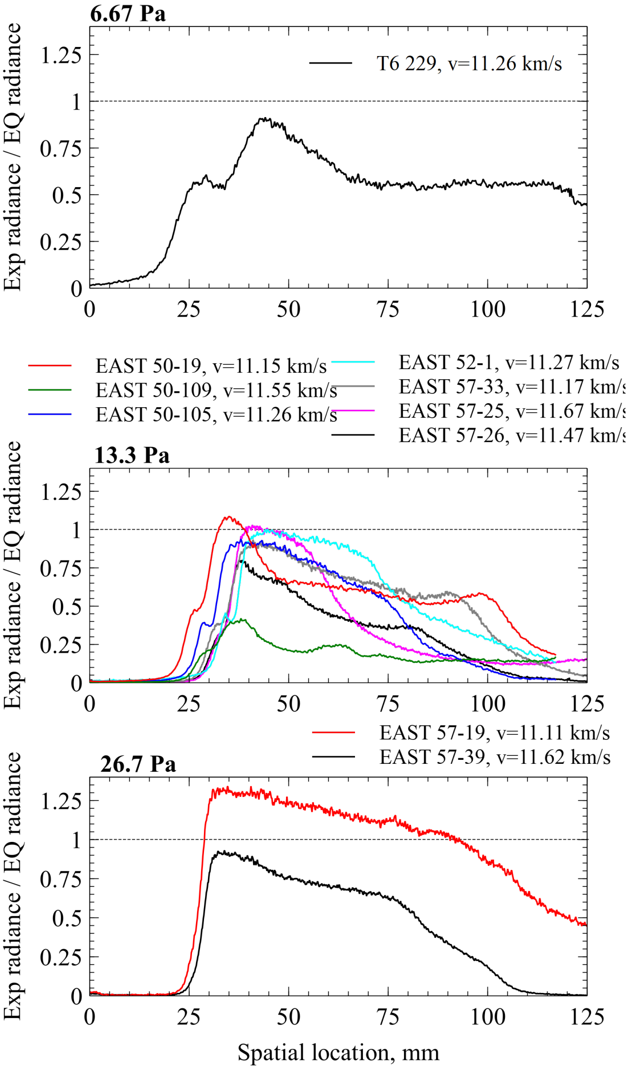

Figure 8. Integrated radiance between 680 nm and 850 nm divided by its respective equilibrium value.

ferent distribution, corresponding to a higher excitation temperature, than states below this energy level. This is reminiscent of what was found for molecular population distributions in an adiabatic reactor due to heavy particle impact [JSP15, TS20]. The referenced investigations excluded electronically excited states and electron impact excitation, which are assumed to dominate the states considered in this study, however a qualitatively similar effect is observed.

Even though the computational non-Boltzmann model presents a better comparison to the experimental data, no satisfactory agreement is achieved, especially considering that the structure of the simulated non-equilibrium region is made of molecular and atomic radiation, while the experiment suggests only atoms contribute to the observed profile. The comparison of simulated and experimental integral radiance profiles can be easily misconstrued resulting in a false positive if the local spectra aren't investigated in detail. The possible causes

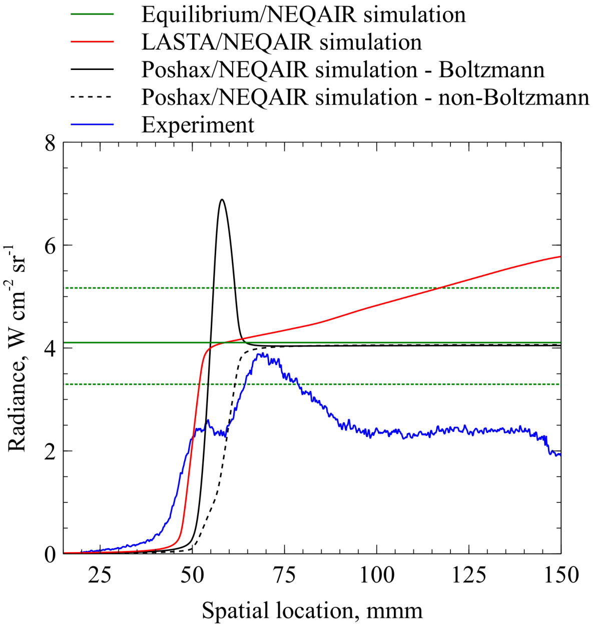

Figure 9. Spatially resolved integrated radiance between 680 nm and 850 nm for shot 229.

for this discrepancy are numerous, including an inadequate thermochemical model [Par93], as suggested by Cruden and Brandis [CB19], an inadequate excitation model, or a larger influence of the shock attenuation as the non-equilibrium region encompasses a the region where LASTA predicts a strong rise in equilibrium temperature.

3.2. Shot 229 - 11.26 km/s, 6.67 Pa

Figure 8 shows the comparison of the data collected in T6 and EAST, normalised by the respective equilibrium radiance. For this freestream pressure, no direct comparison conditions exist that match the velocity. Therefore, higher pressure conditions are shown which feature a similar velocity to the measured 11.26 km/s. There appears to be a trend where lower pressure conditions tend to produce lower radiance than expected. Shot 229 shows about half of the expected equilibrium radiance. Furthermore, the double peak non-equilibrium region becomes much stronger as the pressure is lowered. The feature is not visible at all for conditions at 26.7 Pa, is clearly visible for 13.3 Pa, and very strong at 6.67 Pa. This elongation of non-equilibrium effects is expected as lower pressures lead to fewer collisions after the shock which slows equilibration.

The numerical comparison shown in Fig. 9 reveals that the equilibrium radiance is far below the lower uncertainty bound. In addition, the LASTA simulation predicts a rising radiance profile, contrary to what is observed in the experiment. The Poshax/NEQAIR simulations show a similar trend as in shot 221, with a clear peak for the Boltzmann distributed result and a slow rise of the QSS model. It appears that the experimental measurement may be somewhere in between these estimates, as it shows a slower rise than the Boltzmann model, but with a weaker peak at a later location behind the shock front.

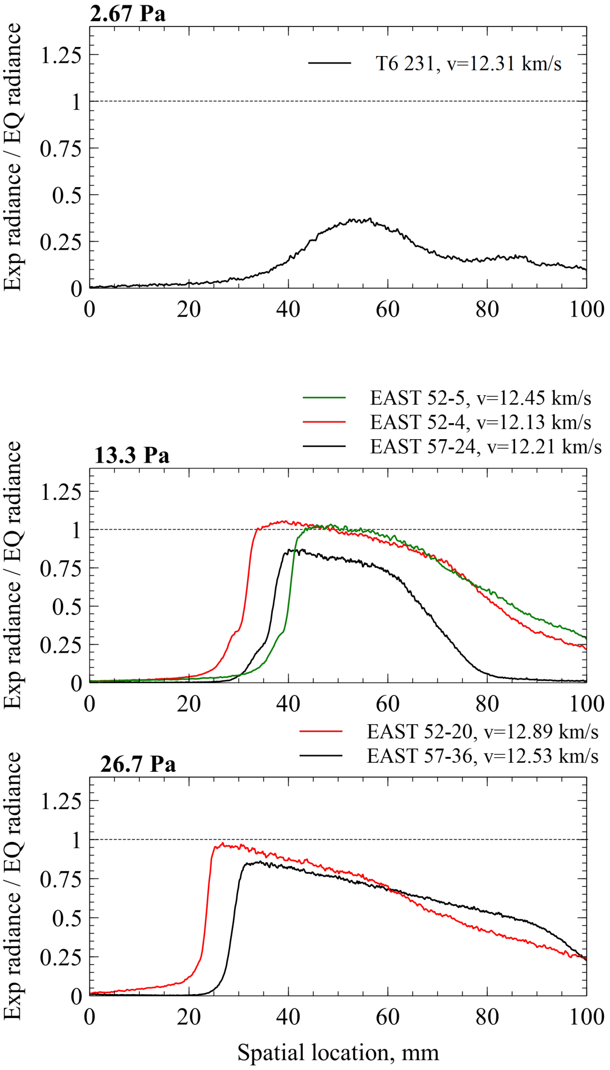

Figure 10. Integrated radiance between 680 nm and 850 nm divided by its respective equilibrium value.

3.3. Shot 231 - 12.31 km/s, 2.67 Pa

Figure 10 shows the respective data for shot 231 and the comparable EAST shots with similar velocities. Similar to the previous case, no directly comparable data exists, and only higher fill pressures are used to compare the datasets from the two facilities. Very similar to shot 229, the non-equilibrium region is greatly elongated as the tube fill pressure is lowered. The measured T6 radiance is far below the expected level of the simulated equilibrium conditions. Figure 11 shows that this is also far below the expected uncertainty bounds for this con-

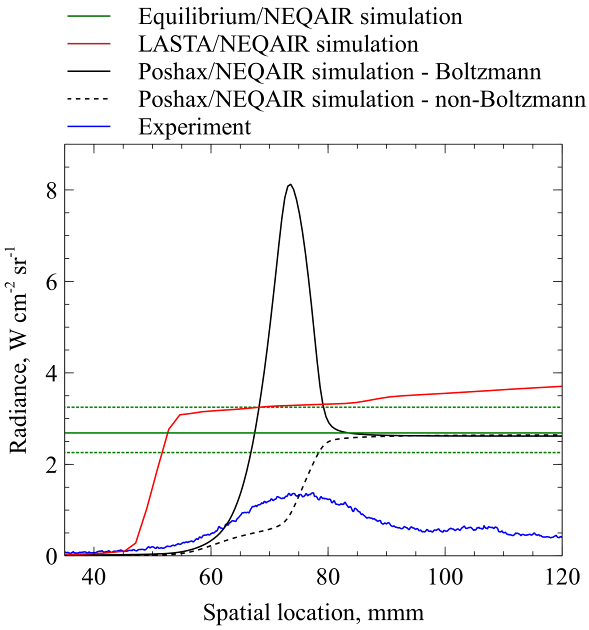

Figure 11. Spatially resolved integrated radiance between 680 nm and 850 nm for shot 229.

dition. The slow rise of the Poshax simulations is due to the slow increase of electron / electronic excitation temperature which drives the processes leading to radiation in this wavelength regime. The experiment shows a gradual increase with a wide peak before the equilibrium region. Clearly, this is different from the predicted Poshax/NEQAIR simulations, be it with a Boltzmann- or a non-Boltzmann distribution.

4. CONCLUSION

This paper presents spectral measurements of spatially resolved radiation behind moving shocks, collected in aluminium shock tube mode of the T6 facility. Spectra are collected in the visible and near infrared region between 680 nm and 850 nm. The data is calibrated for absolute spectral radiance using an integrating sphere and a deuterium lamp respectively. The experimental data is compared to simulations utilising the tools LASTA, Poshax3, and NEQAIR. Qualitative agreement is found between the data collected in T6 and respective data gathered in the EAST facility. However, it is found that the measured radiation for the shock speeds of 11.26 km/s and 12.31 km/s is significantly below expected equilibrium values. As the fill pressure is lowered and velocity increased, this discrepancy is more severe. The simulations reveal that the characteristic double peak is due to an overpopulation of high energy molecular nitrogen states, which is not present in the measured spectra. However, the atomic features of the measured spectra exhibit a behaviour somewhere between the modelled non-Boltzmann and Boltzmann distributed energy states. At this stage, it is inconclusive how the experimental energy state distribution evolves over the shock. The source of discrepancy may also be rooted in the thermochemical rates used which are based on Park's 1993 model. A more clear understanding of the physics through the non-equilibrium region may be obtained by investigating the experimental evolution of atomic high energy states responsible for the emission in the near infrared. In future work, these distribution functions will be analysed to obtain further insight into the flow physics behind the shock front.

5. ACKNOWLEDGEMENT

This research was funded by the UKRI Future Leaders Fellowship scheme (grant number MR/T041269/1), and we extend our gratitude to UKRI. For Open Access, the author has applied a CC BY public copyright licence to any Author Accepted Manuscript (AAM) version arising from this submission.

REFERENCES

[And89] J. D. Anderson. *Hypersonic and High Temperature Gas Dynamics*. McGraw-Hill Book Company, USA, 1989.

[BB19] Khalil Bensassi and Aaron M. Brandis. Time accurate simulation of nonequilibrium flow inside the nasa ames electric arc shock tube. Number 0 in AIAA SciTech Forum. American Institute of Aeronautics and Astronautics, January 2019.

[BC17] Aaron M. Brandis and Brett A. Cruden. Benchmark shock tube experiments of radiative heating relevant to earth re-entry. Number 0 in AIAA SciTech Forum. American Institute of Aeronautics and Astronautics, January 2017.

[BJ14] A. M. Brandis and C. O. Johnston. Characterization of stagnation-point heat flux for earth entry. In *45th AIAA Plasmadynamics and Lasers Conference*, Atlanta, GA, June 2014.

[BJC16] Aaron M. Brandis, Christopher O. Johnston, and Brett A. Cruden. Non-equilibrium radiation for earth entry. Number 0 in AIAA AVIATION Forum. American Institute of Aeronautics and Astronautics, June 2016.

[CB14] Brett A. Cruden and Aaron M. Brandis. Updates to the neqair radiation solver. In *International Workshop on Radiation in High TemperatureGases,*, St. Andrews, Scotland, U.K., 2014. European Space Agency.

[CB19] Brett A. Cruden and Aaron M. Brandis. Measurement of radiative nonequilibrium for air shocks between 7 and 9 km/s. *Journal of Thermophysics and Heat Transfer*, 34(1):154–180, November 2019.

[CBJ17] Brett A. Cruden, Aaron M. Brandis, and Christopher O. Johnston. Development of a radiative heating margin policy for lunar return missions. Number 0 in AIAA SciTech Forum. American Institute of Aeronautics and Astronautics, January 2017.

[CDM19] P Collen, LJ Doherty, and M McGilvray. Measurements of radiating hypervelocity air shock layers in the t6 free-piston driven shock tube. In *ESA FAR conference Monopoli*. ESA Conference Bureau, 2019.

[CDS+21] Peter Collen, Luke J. Doherty, Suria D. Subiah, Tamara Sopek, Ingo Jahn, David Gildfind, Rowland Penty Geraets, Rowan Gollan, Christopher Hambidge, Richard Morgan, and Matthew McGilvray. Development and commissioning of the t6 stalker tunnel. *Experiments in Fluids*, 62(11):225, 2021.

[CMGO09] B. Cruden, R. Martinez, J. H. Grinstead, and J. Olejniczak. Simultaneous vacuum ultraviolet through near ir absolute radiation measurement with spatiotemporal resolution in an electric arc shock tube. In *41st Thermophysics Conference*. AIAA, 2009.

[Cru14] Brett A. Cruden. Absolute radiation measurements in earth and mars entry conditions. In *NATO report*, 2014.

[GCM21] Alex B. Glenn, Peter L. Collen, and Matthew McGilvray. Experimental nonequilibrium radiation measurements for low-earth orbit return. Number 0 in AIAA SciTech Forum. American Institute of Aeronautics and Astronautics, December 2021.

[GM96] S. Gordon and B. J. McBride. Computer program for calculation of complex chemical equilibrium compositions and applications. Reference Publication 1311, NASA, 1996.

[Gol08] Rowan Gollan. *Computational Modelling of High-Temperature Gas Effects with Application to Hypersonic Flows*. PhD thesis, School of Engineering, The University of Queensland, 2008.

[JGL+18] C. M. James, D. E. Gildfind, S. W. Lewis, R. G. Morgan, and F. Zander. Implementation of a state-to-state analytical framework for the calculation of expansion tube flow properties. *Shock Waves*, 28(2):349–377, 2018.

[JMG+13] Christopher O. Johnston, Alireza Mazaheri, Peter Gnoffo, Bil Kleb, and Deepak Bose. Radiative heating uncertainty for hyperbolic earth entry, part 1: Flight simulation modeling and uncertainty. *Journal of Spacecraft and Rockets*, 50(1):19–38, January 2013.

[Joh20] Christopher O. Johnston. Evaluating shock-tube informed biases for shock-layer radiative heating simulations. *Journal of Thermophysics and Heat Transfer*, 35(2):349–361, November 2020.

[JSP15] Richard L. Jaffe, David W. Schwenke, and Marco Panesi. First principles calculation of heavy particle rate coefficients. Number 0 in Progress in Astronautics and Aeronautics, pages 103–158. American Institute of Aeronautics and Astronautics, Inc., January 2015.

[KZB+21] P. V. Kozlov, I. E. Zabelinsky, N. G. Bykova, G. Ya. Gerasimov, V. Yu. Levashov, and Yu. V. Tunik. Experimental study of air radiation behind a strong shock wave. *Acta Astronautica*, 2021.

[LDSFR+20] Mario Lino Da Silva, Ricardo Ferreira, Rafael Rodrigues, Luis Alves, Bruno Gonçalves, Arthur Smith, Jim Merrifield, Victor Villace, and Lionel Marraffa. Qualification of the european shock-tube for high enthalpy research. Number 0 in AIAA SciTech Forum. American Institute of Aeronautics and Astronautics, January 2020.

[MDM+15] Matthew McGilvray, Luke J. Doherty, Richard G. Morgan, David Gildfind, Peter Jacobs, and Peter Ireland. T6: The oxford university stalker tunnel. Number 0 in International Space Planes and Hypersonic Systems and Technologies Conferences. American Institute of Aeronautics and Astronautics, July 2015.

[MEJ+11] Timothy J. McIntyre, Troy N. Eichmann, Carolyn Jacobs, Daniel Potter, Matthew McGilvray, Peter Jacobs, and Richard Morgan. Shock Tube and Expansion Tunnel Measurements of High Temperature Radiating Flows. In H. Lacoste-Francis, editor, *Radiation of High Temperature Gases in Atmospheric Entry*, volume 689 of *ESA Special Publication*, page 37, February 2011.

[Mir66] H. Mirels. Flow nonuniformity in shock tubes operating at maximum test times. *The Physics of Fluids*, 9(10):1907–1912, October 1966.

[Par93] Chul Park. Review of chemical-kinetic problems of future nasa missions. i - earth entries. *Journal of Thermophysics and Heat Transfer*, 7(3):385–398, July 1993.

[Pot11] D. Potter. *Modelling of radiating shock layers for atmospheric entry at Earth and*

Mars. PhD thesis, The University of Queensland, St. Lucia, Australia, May 2011.

[SDMM21] Matthew Satchell, Luca Di Mare, and Matthew McGilvray. Flow nonuniformities behind accelerating and decelerating shock waves in shock tubes. *AIAA Journal*, 60(3):1537–1548, October 2021.

[SGC+21] Matthew Satchell, Alex Glenn, Peter Collen, Rowland Penty-Geraets, Matthew McGilvray, and Luca Di Mare. Analytical method of evaluating nonuniformities in shock tube flows: Application. *AIAA Journal*, 60(2):669–676, November 2021.

[TS20] Erik Torres and Thomas E. Schwartzentruber. Direct molecular simulation of nitrogen dissociation under adiabatic post-shock conditions. *Journal of Thermophysics and Heat Transfer*, 34(4):801–815, May 2020.

[YTSF12] Gouji Yamada, Hiroki Tajayanagi, Toshiyuki Suzuki, and Kazuhisa Fujita. Analysis of shock layer radiation from the vacuum-ultraviolet to near-infrared regions. *Japan Society of Aeronautical Space Sciences Transactions*, 55:60–67, January 2012.